universe

MDPI

Article

The Properties of an Edge-On Low Surface Brightness Galaxies Sample

Tian-Wen Cao [1], Zi-Jian Li [2,3], Pei-Bin Chen [1], Venu M. Kalari [4], Cheng Cheng [2,3], Gaspar Galaz [5], Hong Wu [2] and Junfeng Wang [1,*]

1 Department of Astronomy, Xiamen University, 422 Siming South Road, Xiamen 361005, China; astrocao@xmu.edu.cn (T.-W.C.)
2 National Astronomical Observatories, Chinese Academy of Sciences, Beijing 100101, China
3 Chinese Academy of Sciences South America Center for Astronomy, National Astronomical Observatories, Chinese Academy of Sciences, Beijing 100101, China
4 Gemini Observatory/NSFs NOIRLab, Casilla 603, La Serena 1700000, Chile
5 Instituto de Astrofisica, Pontificia Universidad Católica de Chile, Av. Vicuña Mackenna 4860, Santiago 7820436, Chile
* Correspondence: jfwang@xmu.edu.cn

Abstract: We analyzed the properties of a sample of edge-on low-surface brightness galaxies, which are referred to as Cao23 ELSBGs. Cao23 ELSBGs exhibit a wide range of luminosities ($-22 < M_r < -13$) with a mean scale length of 3.19 ± 1.48 kpc. Compared to HI-rich dwarf ELSBGs, Cao23 ELSBGs display more extended disk structures and redder (g-r) colors. They are also, on average, more massive than HI-rich dwarf ELSBGs. Star formation rates (SFRs) were calculated using WISE 12 μm luminosity conversions and spectral energy distribution (SED) fitting methods, respectively. Cao23 ELSBGs fall below the main sequence with specific star formation rates (sSFRs) primarily in the range of 0.01–0.1 Gyr^{-1}. More massive Cao23 LSBGs tend to have lower sSFRs. Additionally, we derived the non-parametric star formation histories (SFHs) of Cao23 ELSBGs by SED fitting, dividing the SFHs into seven look back time bins with constant SFRs assumed for each bin. Our analysis indicates that high-mass ($M_* > 10^{9.0}\ M\odot$) Cao23 ELSBGs assembled their mass earlier than their lower-mass counterparts, supporting a downsizing trend for LSBGs.

Keywords: low surface brightness galaxies; star formation; star formation history

Citation: Cao, T.-W.; Li, Z.-J.; Chen, P.-B.; Kalari, V.M.; Cheng, C.; Galaz, G.; Wu, H.; Wang, J. The Properties of an Edge-On Low Surface Brightness Galaxies Sample. *Universe* **2024**, *10*, 432. https://doi.org/10.3390/universe10110432

Academic Editor: Andrea Lapi

Received: 14 October 2024
Revised: 15 November 2024
Accepted: 18 November 2024
Published: 20 November 2024

1. Introduction

Low surface brightness galaxies (LSBGs) are characterized by their extremely faint structure with a central surface brightness (μ_0) of the disk lower than 22.0–23.0 mag $arcsec^{-2}$ in the B-band [1–9]. LSBGs encompass various galaxy types, including dwarf LSBGs [10], ultra-diffused galaxies (UDGs) characterized by the effective surface brightness $\mu_e \geqslant 24$ mag $arcsec^{-2}$ and the effective radius $R_e \geqslant 1.5$ kpc [11,12], and giant LSBGs (GLSBGs) with radii up to 130 kpc and stellar masses of the order of $10^{11}\ M_\odot$, as exemplified by Malin 1 [13–18]. The stellar masses of LSBGs exhibit a wide range, spanning from dwarf LSBGs to GLSBGs. The faint features of LSBGs are related to their low-surface stellar mass densities [19]. LSBGs are metal-poor [20–22]. In the mass-metallicity ($M_* - Z$) relation, LSBGs show a flatter trend compared to star-forming galaxies, suggesting inefficient oxygen abundance enhancement [23]. Furthermore, LSBGs display lower star formation rates (SFRs) than the main sequence galaxies [24–26].

LSBGs typically exhibit lower dust content compared to high surface brightness galaxies [27], and their far-infrared emissions are weaker than those of normal star-forming galaxies [28]. Among five GLSBGs, only UGC 6614 and UGC 6151 show 160 μm (cool) dust emission in [28] with the dust mass of UGC 6614 measured at $10^{8.42} M_\odot$ [27]. Ref. [29] have discussed the higher dust content in some extreme GLSBGs. Additionally,

LSBGs are characterized by a shortage of molecular gas [30,31]. Ref. [32] estimated the molecular gas surface density in Malin 1 to range from approximately 2 to 0.8 $M_{\odot} pc^{-2}$ with a very low molecular-to-atomic gas mass ratio. Parts of LSBGs are HI-rich [33], exhibiting higher HI gas mass fractions ($f_{HI} = M_{HI}/M_{*}$) than those in the HI-selected spiral galaxies in the HI Parkes All Sky-Survey Catalogue (HICAT) and the Wide-field Infrared Survey Explorer (WISE) sample from [34]. The spiral galaxies in [34] are high surface brightness systems. Many LSBGs are late-type (Sc and later) spiral galaxies with amorphous or fragmentary and faint spiral patterns, and some are similar to irregular galaxies [33]. Some GLSBGs generally exhibit clearly defined spiral structures [35]. The differences between gas-rich and gas-poor LSBGs are not clear. Our current understanding of various LSBG properties remains limited. The origins and evolutions of these LSBGs are under debate [36–39]. The typical formation scenario is that LSBGs arise in haloes with high angular momentum under the ΛCDM framework [40,41]. Other scenarios also considered in recent research, such as ram-pressure stripping [42], extreme feedback processes [43], and mergers [22,44–47].

The star formation history (SFH) is an essential parameter tracing the stellar assembly history and thereby revealing the evolutionary pathway of galaxies. The specific star formation rate (sSFR) at different redshifts and the observed spectral energy distributions (SEDs) can provide valuable insights into SFH. The sSFR, defined as the ratio of SFR to stellar mass (M_{*}) [48], reflects the rate ratio of new stars to the assembled ga;axy mass [49]. Estimating the sSFR at different redshifts [50,51] offers a deeper understanding of the galaxy's star formation history. The sSFR–stellar mass relation exhibits a steeper trend at high redshift [52] for main sequence galaxies. It indicates that the massive galaxies have assembled their stellar mass at the early time, which is a concept known as downsizing [53]. Very few studies have explored LSBGs at high redshifts [54,55]. The topic of SFH of LSBGs is a rarely mentioned area [10,25], and the relevant discussion is based on the HI-gas depletion time ($t_{dep} = M_{HI}/\mathrm{SFR}$, [56]). Ref. [25] demonstrated that the current SFRs of their HI-detected LSBGs are close to average SFRs in Hubble time by the HI depletion time t_{dep}-sSFR relation, suggesting that most LSBGs are stable systems.

Ref. [23] presented a sample of 330 blue edge-on low-surface brightness galaxies (ELSBGs) with SDSS fiber spectra and analyzed the chemical evolution of this sample. The ELSBGs in [23] have distance information, which is often unavailable in most optically selected LSBG samples. Additionally, the ELSBGs show higher projected surface stellar mass densities than face-on LSBGs, making it possible to obtain high-quality integral field spectroscopy (IFS) data. This enables detailed investigations into their perpendicular disk structure providing insights into the formation and evolution of LSBGs through dynamical studies. For instance, ref. [22] presented IFS observations of an ELSBG (AGC 102004) from [23] and discussed evidence for a minor or mini-merger event in AGC 102004.

In this study, we investigate properties of the ELSBGs from [23], focusing on SFR, sSFR, t_{dep}, and non-parametric SFH. We give a review of ELSBGs from [23] in Section 2 and compare ELSBGs with previous ELSBG samples (HI-rich dwarf ELSBGs and super-thin galaxies) in Section 3. In Section 4, we examine the SFR of ELSBGs based on multi-band data, and in Section 5, we assess their HI gas depletion times. The SFH of ELSBGs inferred from the non-parametric model using the SED fitting code PROSPECTOR is represented in Section 6. We summarize our findings in Section 7. Throughout this paper, we utilize AB magnitudes for all measurements. We adopt a ΛCDM cosmology with $\Omega_m = 0.3$, $\Omega_\Lambda = 0.7$, $H_0 = 70\,\mathrm{km\,s^{-1}\,Mpc^{-1}}$. In this paper, the stellar masses of ELSBGs are from the MPA-JHU catalog [57], and the redshifts of ELSBGs are SDSS spectroscopic redshifts. We use the Chabrier universal initial mass function (IMF, [58]) throughout the article. We convert Salpeter IMF [59] and Kroupa IMF [60] with the following conversion factors: $\mathrm{SFR}^{cha} = \mathrm{SFR}^{sal}/1.41$ [61–63], $\mathrm{SFR}^{cha} = \mathrm{SFR}^{kro} \times 0.943$ [64].

2. Cao23 ELSBGs

The ELSBGs' sample is drawn from [23], including 330 blue ELSBGs with SDSS spectra. The initial edge-on galaxies sample is from [65]. The ELSBGs sample are selected based on their face-on mean surface brightness in 3″ radius (μ_{3-face}) in a g-band lower than 25 mag arcsec^{-2} and the projected (u-r) color in the center 3″ aperture region below the green valley upper boundary [66]. The details of conversion from edge-on to face-on surface brightness estimation are given in [23]. The final 330 ELSBGs show the face-on center surface brightness (μ_{0-face}) ranges from 22.34 to 23.75 mag arcsec^{-2} and redshifts from 0.0026 to 0.14. Hereafter, we refer to the ELSBGs from [23] as "Cao23 ELSBGs".

We separate Cao23 ELSBGs into five bins according to their inclination angle and test how the inclination angle affects the surface brightness correction for edge-on galaxies with the method from [67–70] due to deviations from a 90-degree inclination angle. We show the relationship between the mean value of the scale height to scale length ratio ($-2.5 \times \log(h_s/r_s)$) and the inclination angle of Cao23 ELSBGs in Figure 1. The h_s and r_s are from the GALFIT edge-on disk model fitting [23], and the inclination angle is from [65]. It shows a weak trend that the $-2.5 \times \log(h_s/r_s)$ increases with the inclination angle increasing and $-2.5 \times \log(h_s/r_s)$ does not change too much with respect to Cao23 ELSBGs. It suggests that the inclination angle does influence the surface brightness correction, but the influence is not significant for inclination angle $> 81°$. The inclination angle $> 81°$ contributes 86% of Cao23 ELSBGs which does not significantly affect the main results of the sample.

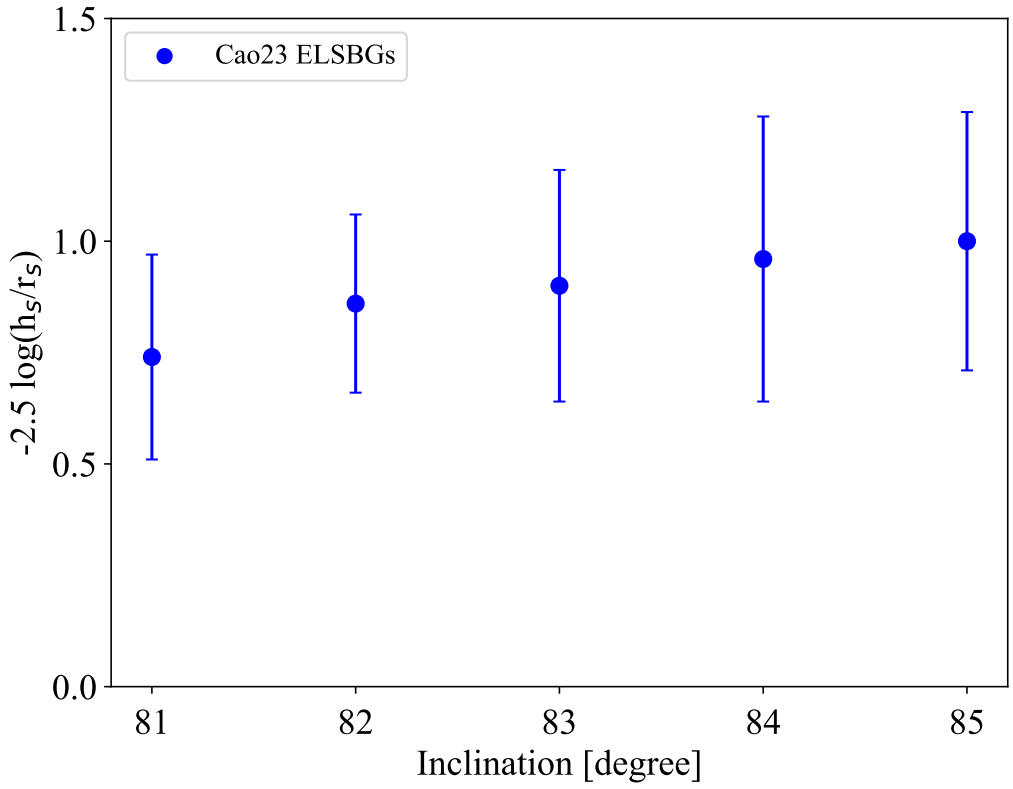

Figure 1. The relationship between the mean value of the scale height to scale length ratio ($-2.5 \times \log(h_s/rr_s)$) and inclination. We note the $-2.5 \times \log(h_s/r_s)$ is the correction factor from the observed center surface brightness to face-on center surface brightness for edge-on cases [70].

The selection of the LSBG sample usually excludes those high ellipticity ($\epsilon = (1 - b/a) \geq 0.7$, a and b are the semi-major axis and semi-minor axis, respectively) targets to avoid the edge-on galaxies, high redshift, spurious artifacts, and galaxy blends [33,71,72]. It is worth noting that the surface brightness cutting sometimes does not account for inclination angle correction [71,72], which may result in parts of ELSBGs being missed in this step.

Recent studies [70] have shown that a significant portion of ELSBGs would be overlooked if inclination effects are not considered. Furthermore, the number of highly inclined galaxies is less than in other cases. These factors collectively contribute to the rarity of ELSBGs in LSBGs. This limitation may introduce biases in studies of the intrinsic morphology of LSBGs.

3. Comparison with Other ELSBG Samples

We compare the physical parameters of Cao23 ELSBGs with two other ELSBGs samples: HI-rich dwarf ELSBGs from [70] and super-thin galaxies from [73]. Both studies provide comparisons between edge-on ELSBGs and other LSBGs, concluding that ELSBGs exhibit similar properties to other LSBGs.

3.1. HI-Rich Dwarf ELSBG Sample

Ref. [70] present 281 HI-rich dwarf ELSBGs from the crossmatch between Sloan Digital Sky Survey Data Release 7 and the 40% ALFALFA catalog. They require the b/a ≤ 0.3 in the SDSS g-band or r-band to select edge-on galaxies. They compare their ELSBGs with face-on HI-rich dwarf LSBGs from [33] and conclude that the differences between edge-on and face-on LSBGs tend to be much smaller.

We compare the physical parameters of Cao23 ELSBGs with these HI-rich dwarf ELSBGs. We use the same method with [70] to obtain $\mu_{0_{face}}$ in Figure 2a. Cao23 ELSBGs show slightly fainter $\mu_{0_{face}}$ (with the mean $\mu_{0_{face}}$ value 22.89 $\pm$ 0.51 mag arcsec^{-2}) than HI-rich dwarf ELSBGs (with the mean $\mu_{0_{face}}$ value 22.67 $\pm$ 0.47 mag arcsec^{-2}). The mean value of b/a of Cao23 ELSBGs and HI-rich dwarf ELSBGs is 0.20 $\pm$ 0.06 and 0.18 $\pm$ 0.08, respectively.

The g-band absolute magnitude of HI-rich dwarf ELSBGs is much fainter than that of the Cao23 ELSBGs in Figure 2c. The mean value of M_g for Cao23 ELSBGs and HI-rich dwarf ELSBGs is -19.36 ± 0.85 mag and -16.63 ± 1.12, respectively. Cao23 ELSBGs are selected with SDSS fiber spectra, which leads to faint targets being missed. The difference in luminosity reflects the varying mass distributions between the two samples. These HI-rich dwarf LSBGs are mainly occupied by low-mass galaxies ($<10^9$ $M_\odot$, [35]), while the Cao23 ELSBGs are, on average, more massive.

The scale length (r_s) of Cao23 ELSBGs is larger than that of HI-rich dwarf ELSBGs. The mean value of r_s of Cao23 ELSBGs is 3.19 $\pm$ 1.48 kpc, while for HI-rich dwarf ELSBGs, it is 1.84 $\pm$ 0.89 kpc. HI-rich LSBGs are primarily composed of dwarf LSBGs [33,70], indicating that they are likely small galaxies.

We compare the observed (g-r) color for two ELSBG samples in Figure 2e. Cao23 ELSBGs are redder in (g-r) color than HI-rich dwarf ELSBGs. The mean value of (g-r) of Cao23 ELSBGs and HI-rich dwarf ELSBGs is 0.46 $\pm$ 0.16 and 0.34 $\pm$ 0.11, respectively.

Overall, Cao23 ELSBGs show slightly fainter surface brightness, more extended disk structure, and redder color than HI-rich dwarf ELSBGs from [70]. The redder color and larger r_s of Cao23 ELSBGs are consistent with Cao23 ELSBGs being on average more massive.

3.2. Super-Thin Galaxies Sample

Ref. [73] present a sample of super-thin (ST) galaxies with b/a of 0.05–0.1 and no bulge component (the center surface brightness in B-band (μ_B) > 23.0). A comparison LSBG sample with $\mu_B > 23.0$ also is included in [73]. Ref. [73] compares the SFR of STs and LSBGs by different methods and conclude that STs and LSBs have equal intrinsic SFR, which possibly implies STs are just the LSBGs seen edge-on.

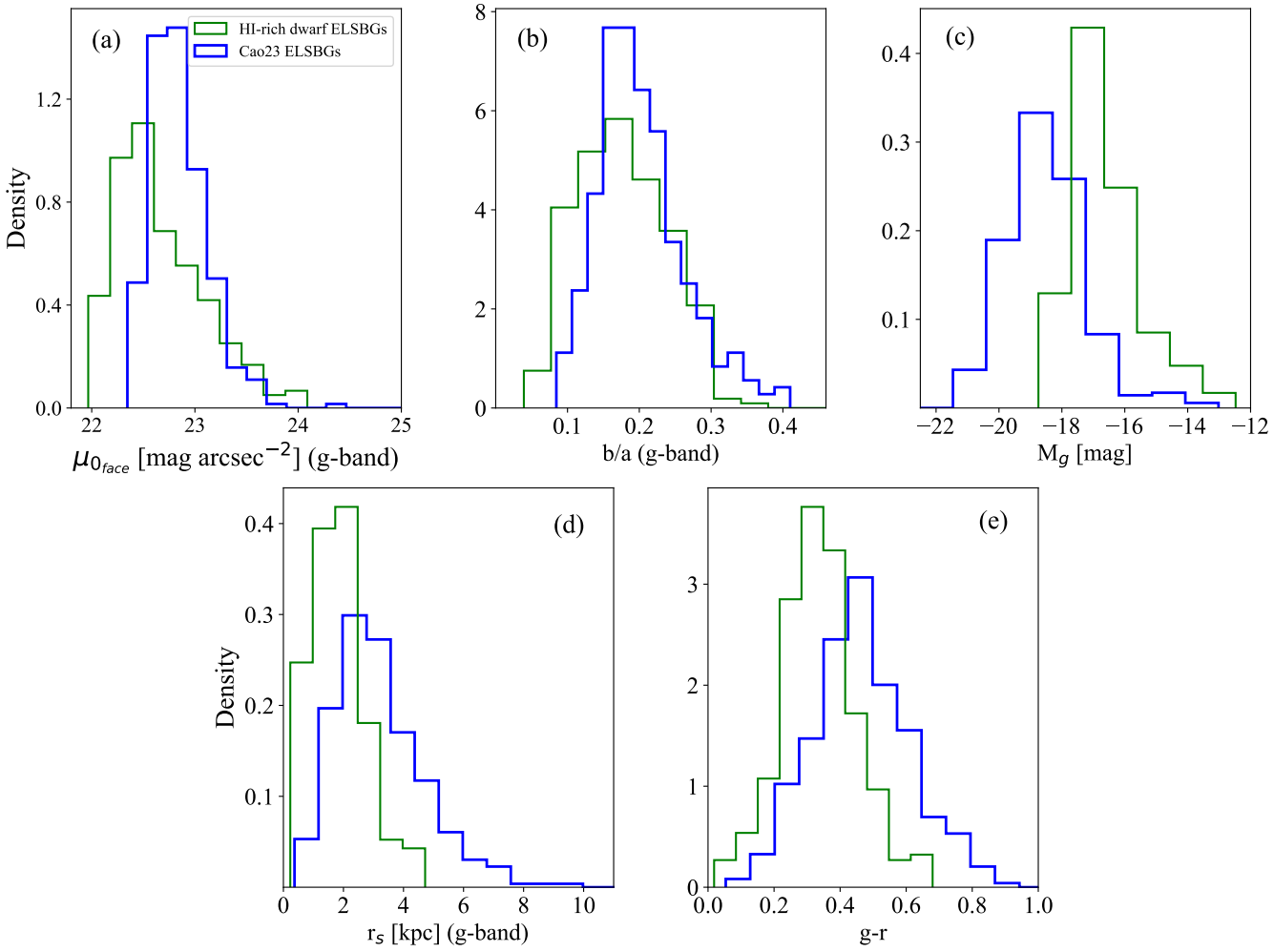

Figure 2. Panel (**a**): The distribution of $\mu_{0_{face}}$ in g-band. Panel (**b**): The distribution of axis ratio (b/a) in g-band. Panel (**c**): The distribution of g-band absolute magnitude. Panel (**d**): The distribution of scale length (r_s) of g-band in the unit of kpc. Panel (**e**): The distribution of (g-r) color. The blue and green line represents Cao23 ELSBGs and HI-rich dwarf ELSBGs from [70] in all panels, respectively.

Cao23 ELSBGs show a comparable distribution of M_r with the STs and LSBGs' sample for $M_r < -17$ mag in Figure 3a.

We compare the SFR of Cao23 ELSBGs with those of STs and LSBGs. We apply the same code (Multi-wavelength Analysis of Galaxy Physical Properties, MAGPHYS [74]) to obtain SFR as [73]. Ref. [73] used ten bands of photometric data from 0.15 to 2.2 µm for SED fitting. We require that Cao23 ELSBGs have observation data in GALEX: FUV, NUV, SDSS: u,g,r,i,z, and WISE: W1, W2, and a signal-to-noise ratio (SNR) larger than five in W2, and they also keep consistent the similar wavelength coverage of [73]. Overall, 192 Cao23 ELSBGs meet the requirement. We use the model magnitude associated with de Vaucouleurs and exponential model fits in each band to avoid pollution from the nearby targets. The SEDs cover the rest-frame wavelength ranges from FUV to NIR (from 0.15 to 4.6 µm) for Cao23 ELSBGs. This subsample is also used in Sections 4 and 6.

Stellar population synthesis is used to predict the observed SED [75] and model the spectral evolution of the stellar population with an IMF. The IMF is assumed [58]. The IMF and the dust attenuation of the stellar spectrum are modeled using the two-component model of [76] in MAGPHYS code. The exponentially declining SFH model is parametrized as SFR(t) $\propto \exp(-\gamma t)$, which is characterized by an age t_{gal} of the galaxy and star formation time-scale γ^{-1}, and random bursts are set to occur with equal probability at all times [77].

We show the Stellar Mass-SFR (M_*-SFR) relation in Figure 3b of 75 Cao23 ELSBGs with reduced χ^2 values smaller than five. The $SFR_{MAGPHYS}$ distribution of Cao23 ELSBGs with a median value of 0.22±0.55 is consistent with that of STs ($0.2^{+0.9}_{-0.2}$). The LSBGs in Figure 3b show a wide range and have larger $SFR_{MAGPHYS}$ (with median value $0.4^{+2.2}_{-0.3}$) than that of Cao23 ELSBGs and STs on average. The range of $sSFR_{MAGPHYS}$ for Cao23 ELSBGs is from 0.01 to 0.1 Gyr^{-1}.

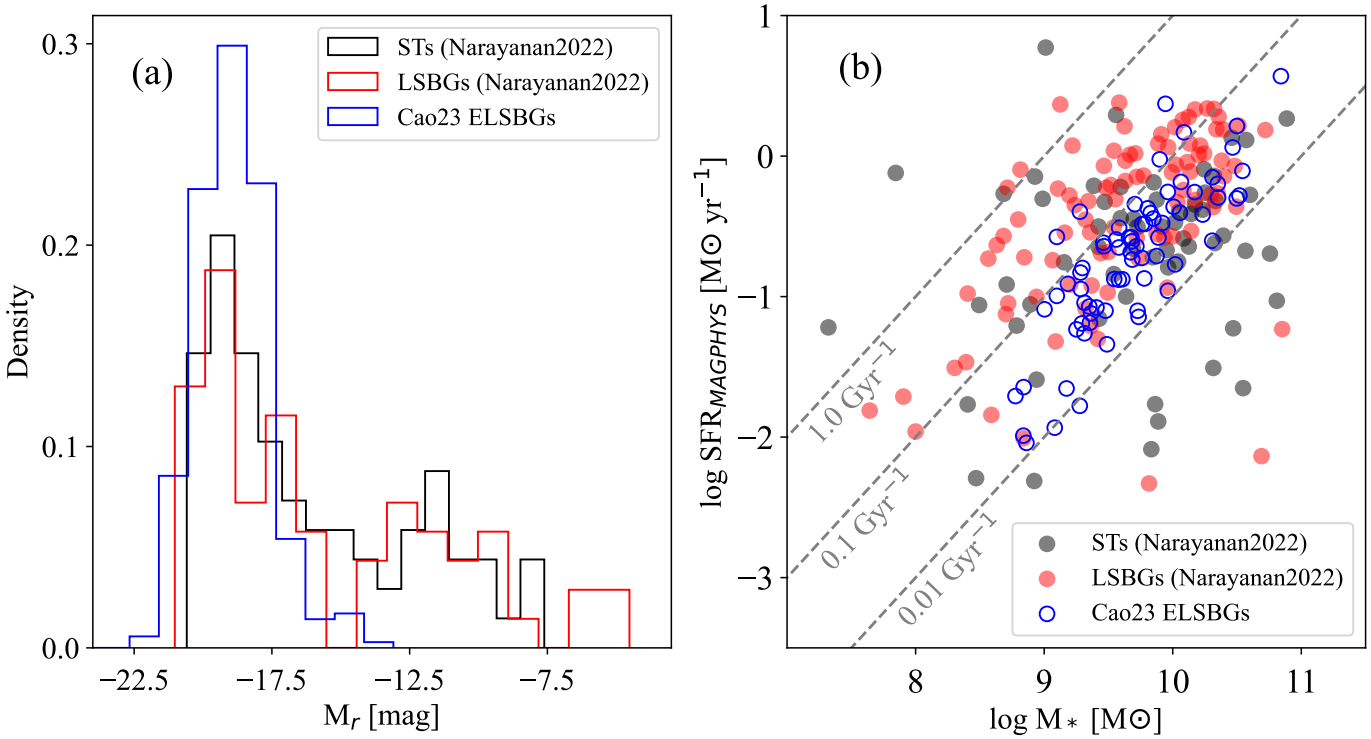

Figure 3. Panel (**a**): The distribution of M_r of Cao23 ELSBGs (blue line), STs (black line) [73], and LSBGs (red line) [73]. Panel (**b**): The M_*-SFR relation of Cao23 ELSBGs (open blue circles), STs (gray dots) [73], and LSBGs (red dots) [73]. The gray dashed lines, arranged from bottom to top, correspond to specific specific star formation rates (sSFRs) of 0.01 Gyr^{-1}, 0.1 Gyr^{-1}, and 1 Gyr^{-1}.

4. SFR of Cao23 ELSBGs

We use the infrared luminosity of WISE W3 12 μm and the SED fitting method to estimate the SFR for Cao23 ELSBGs. The W3 luminosity traces the emission from polycyclic aromatic hydrocarbon (PAHs), which is well related with the star formation rate [78]. And W3 luminosity–SFR conversion is not affected by dust attenuation. However, since only one third of our sample has high SNR W3 photometries, we also obtain the SFRs through composite stellar population synthesis.

4.1. SFR Derived from W3 Luminosity

The 131 Cao23 ELSBGs show WISE W3 12 μm detection with SNR values larger than three. The redshifts of Cao23 ELSBGs are smaller than 0.14, and we have ignored the k-correction. For most of our object, our treatment of observed 12 μm flux as an SFR estimator will induce less than 10% error, which is small compared with the photometric error. We derive SFR_{W3} following the formula form [79,80]:

$$logSFR_{W3} = 0.66 \times (logL_v(W3) - 22.5) + 0.16 \quad (1)$$

with L_v(W3) in W Hz^{-1} and [58] IMF.

Figure 4 shows the SFR_{W3} and $sSFR_{W3}$ of 131 Cao23 ELSBGs. Overall, Cao23 ELSBGs deviate from the main sequence (MS) and around the 50% level of the MS line. The MS line

in Figure 4 is according to SFR_{W3}. We note that the MaNGA edge-on sample was selected based on two considerations: edge-on inclination and no clear evidence for ongoing major merging interaction [80]. The SFR_{W3} and $sSFR_{W3}$ of the MaNGA edge-on sample show a wider range than that of the Cao23 ELSBGs in Figure 4. The typical error is the mean value of the SFR_{W3} error, which is derived from the W3 band magnitude error.

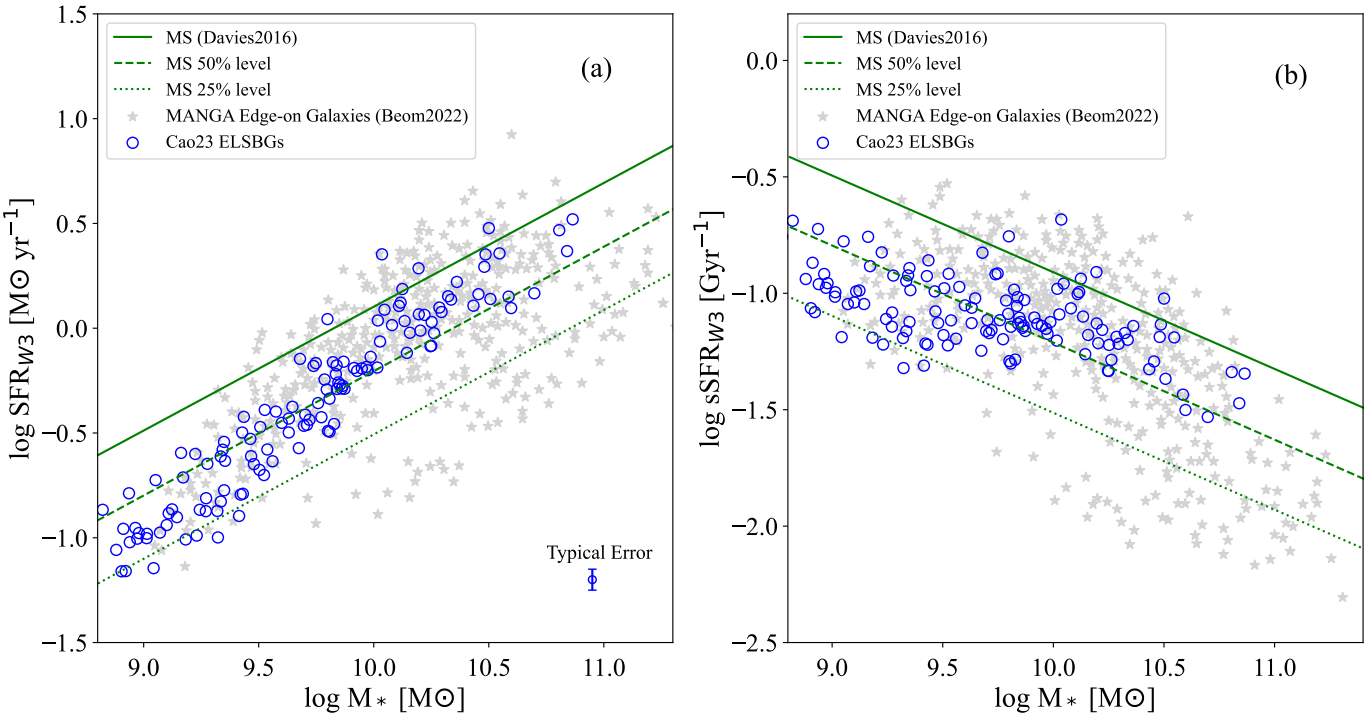

Figure 4. Panel (**a**): SFR_{W3} versus M_* of 131 Cao23 ELSBGs (open blue circles) and MaNGA 472 edge-on galaxies (gray stars) from [80]. The typical error is the mean value of the SFR uncertainty derived from the W3 magnitude error. Panel (**b**): $sSFR_{W3}$ versus M_* of 131 Cao23 ELSBGs (open blue circles) and MaNGA 472 edge-on galaxies (gray stars) from [80]. The green line represents the main sequence line for star-forming nearby galaxies with SFR derived from W3 luminosity [79,80]. The dashed and dotted lines indicate 50% and 25% levels of the main sequence lines from [80].

4.2. SFR Derived from CIGALE

We apply the Code Investigating GALaxy Emission (CIGALE, [81,82]) to perform the SED fitting and estimate SFRs of 192 Cao23 ELSBGs (multi-band data from GALEX (FUV, NUV), SDSS (u,g,r,i,z), and WISE (W1, W2). The SEDs cover the rest-frame wavelength from 0.15 to 4.6 μm).

The stellar population synthesis models are from [75] with a [58] IMF. We set the stellar metallicities of 0.0001, 0.0004, 0.004, and 0.008. We employed the delayed star formation history (SFH) model consistent with [83]. The dust emission model is from [84] and the dust attenuation is modified [85] attenuation law. The details of the input parameters set are listed in Appendix A Table A1.

We use the likelihood-weighted mean SFR from the CIGALE results in Figure 5. The typical error is the mean value of the SFR_{cigale} error from CIGALE outputs. Cao23 ELSBGs show a distribution of $sSFR_{cigale}$ in the range of 0.01–0.1 Gyr^{-1} in Figure 5. Different types of LSBGs (UDGs, HI-rich UDGs, dwarf LSBGs and GLSBGs) are also shown in Figure 5. It shows a large scatter in the M_*-SFR relation for those LSBGs with $M_* < 10^{8.5}$ $M_\odot$. Part of the HI-rich dwarf LSBGs from [33] shown in [35] exhibit sSFRs larger than 0.1 Gyr^{-1} and show a larger SFR than Cao23 ELSBGs overall, which means those HI-rich dwarf LSBGs tend to have a larger SFR value. We note the SFR derived from different methods, and sample selection bias would induce the scatter in the M_*-SFR relation.

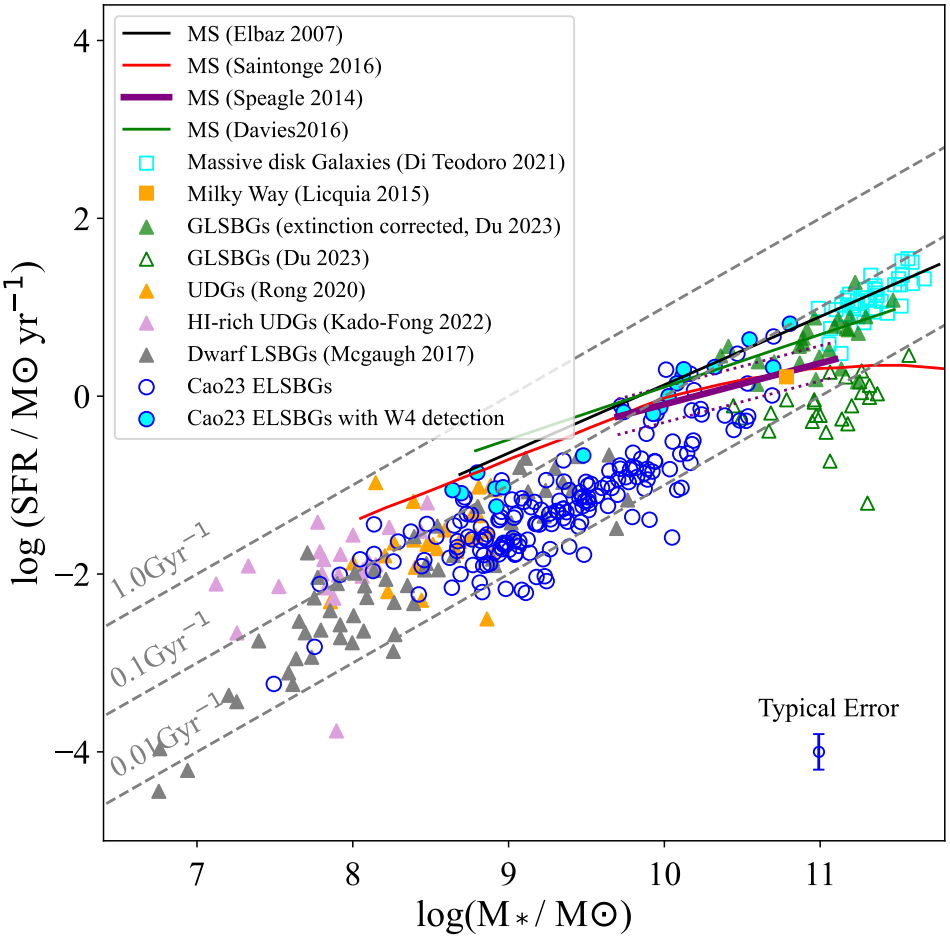

Figure 5. The M_*-SFR relation. Blue open circles denote Cao23 ELSBGs and blue open circles with filled cyan color are those Cao23 ELSBGs with W4 detecion. Gray triangles represent dwarf LSBGs from [10], orange triangles distinguish UDGs from [86], and purple triangles are HI-rich UDGs from [83]. Green filled and unfilled triangles are GLSBGs from [35] with dust extinction correction and none correction, respectively. The orange and open cyan squares are the Milky Way [35] and Massive disk galaxies [87], respectively. The purple line, black line, and red line represent the main sequence from [61,88,89]. The green line represents the main sequence line for star-forming nearby galaxies with the SFR derived from W3 luminosity [79,80]. The gray dashed lines, arranged from bottom to top, correspond to specific star formation rates (sSFRs) of 0.01 Gyr^{-1}, 0.1 Gyr^{-1}, and 1 Gyr^{-1}. The typical error is the mean value of the SFR error from CIGALE. The IMF has been corrected to Chabrier IMF for all data points.

The variable integrated galactic initial mass function (IGIMF) has been mentioned in [56,90,91]. The IGIMF systematically varies with the global SFR and metallicity and also affects the MS [92]. Ref. [92] shows that estimates of the SFRs for local star-forming galaxies differ by factors of approximately 10 between the IGIMF theory to the canonical universal IMF, particularly at the low-mass end. Cao23 ELSBGs primarily include massive galaxies ($M_* > 10^{9.0}\ M_\odot$), and the difference for those massive ones are small in [92]. Additionally, the lack of far-infrared data in the SED fitting may impact results, as noted by [93]. Ref. [94] estimated that using only stellar SEDs (sampling starlight from 0.4 to 2.2 μm) introduces an uncertainty of about 0.3 dex. However, this does not affect the main results in Figure 5, which show that Cao23 ELSBGs lie below the MS.

5. HI-Gas Content and t_{dep}

We compare the HI-gas content and depletion time t_{dep}, which characterizes the evolutionary status of star formation for HI-rich and normal dwarf LSBGs in Figure 6.

Figure 6a shows the relation between HI gas mass (M_{HI}) and M_*. The HI-rich UDGs display higher M_{HI} values than the dwarf LSBGs at similar stellar masses. Among the Cao23 ELSBGs, 75 have HI detections [23] and belong to HI-rich ones. Figure 6b presents the relation between t_{dep} and sSFR. The SFRs of both dwarf LSBGs [10] and HI-rich dwarf LSBGs [25] are derived from Hα luminosities, and both share a similar stellar mass range. The parent sample of HI-rich dwarf LSBGs is from [33]. The HI-rich dwarf LSBGs exhibit higher sSFR and shorter t_{dep} than low-HI-fraction dwarf LSBGs, indicating that a higher HI gas content correlates with a higher SFR. We also show that 35 Cao23 ELSBGs with HI detection also show in Figure 6b. Additionally, 35 Cao23 ELSBGs with HI detection are located close to dwarf LSBGs but are, on average, more massive. This trend is evident in Figure 7.

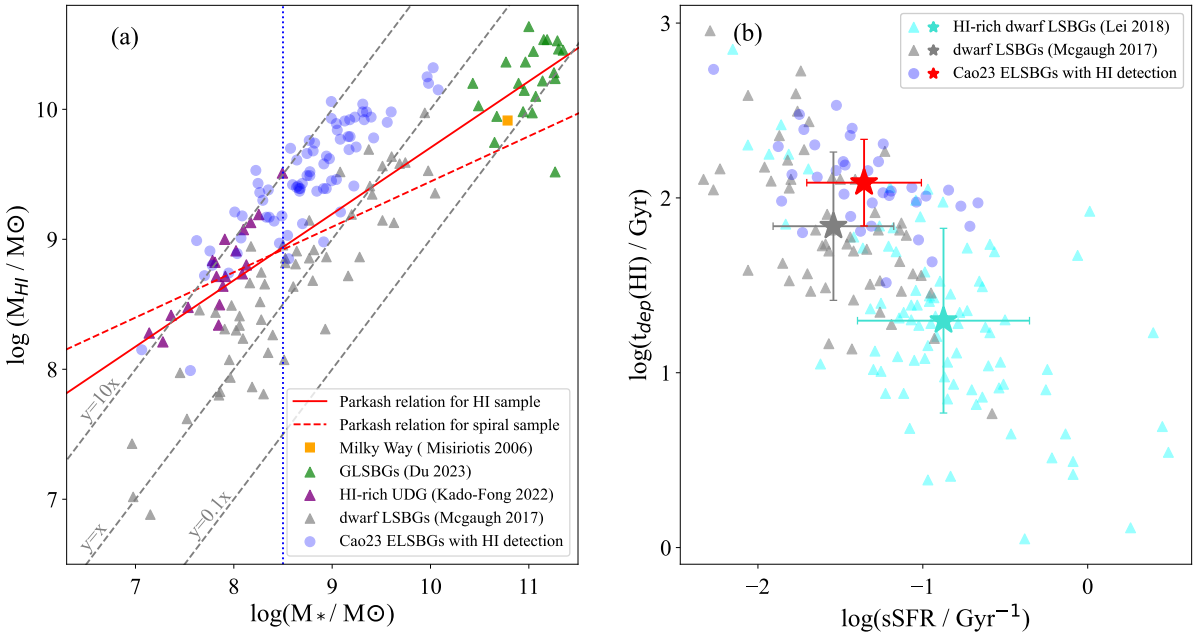

Figure 6. Panel (**a**): The M_{HI}-M_* relation for LSBGs. Blue filled circles denote Cao23 ELSBGs with HI detection, gray triangles represent dwarf LSBGs from [10], and purple triangles distinguish UDGs from [83]. Green filled triangles are GLSBGs from [35]. The orange square represents the Milky Way. The red solid line represents the relation followed by the HI-selected sample of galaxies with a 1σ scatter of 0.5 dex, and the red dashed line shows the relation followed by the spiral galaxies out of the M_*-selected sample with a 1σ scatter of 0.4 dex from [34]. Panel (**b**): The t_{dep} (HI) vs. sSFR diagram of LSBGs. Blue filled circles denote Cao23 ELSBGs with HI detection, gray triangles denote dwarf LSBGs from [10], and cyan triangles indicate HI-rich dwarf LSBGs from [25]. The red star symbol is the mean value of Cao23 ELSBGs, while the gray and cyan stars represent the mean values for dwarf LSBGs and HI-rich dwarf LSBGs, respectively.

We show the sSFR and M_* (sSFR-M_*) relation in Figure 7. The sSFR values of Cao23 ELSBGs derived from SFR$_{\rm cigale}$. The sSFR values for the majority of Cao23 ELSBGs fall in the range of 0.1 to 0.01 Gyr^{-1}. Notably, a subset of ELSBGs exhibits higher sSFR values exceeding 0.1 Gyr^{-1}. Thirty-five Cao23 ELSBGs with HI detection show average higher sSFR values to other Cao23 ELSBGs. The sSFR shows a large scatter below $10^{8.5}$ $M_\odot$ in Figure 7. The sSFR values of dwarf LSBGs [10] show a systematically lower sSFR than those of HI-rich UDGs [83] when considering stellar masses below $10^{8.5}$ $M_\odot$. Specifically, the mean sSFR for dwarf LSBGs and HI-rich UDGs with M$_*$ $< 10^{8.5}$ $M_\odot$ stands at 0.04 and 0.16 Gyr^{-1}, respectively. GLSBGs and/or massive Cao23 ELSBGs on average have lower sSFR values in Figure 7.

HI-rich dwarf LSBGs exhibit higher sSFRs than the low-HI-gas fractions dwarf LSBGs at the low-mass end. The authors of [31] explored the molecular gas content in nine

HI-rich LSBGs and found that these galaxies may have higher star formation efficiency (SFE; defined as SFR/M_{H_2}) compared to typical star-forming galaxies. This suggests that HI-rich dwarf LSBGs may contain more molecular gas than low-HI-fraction dwarf LSBGs, contributing to their elevated sSFR.

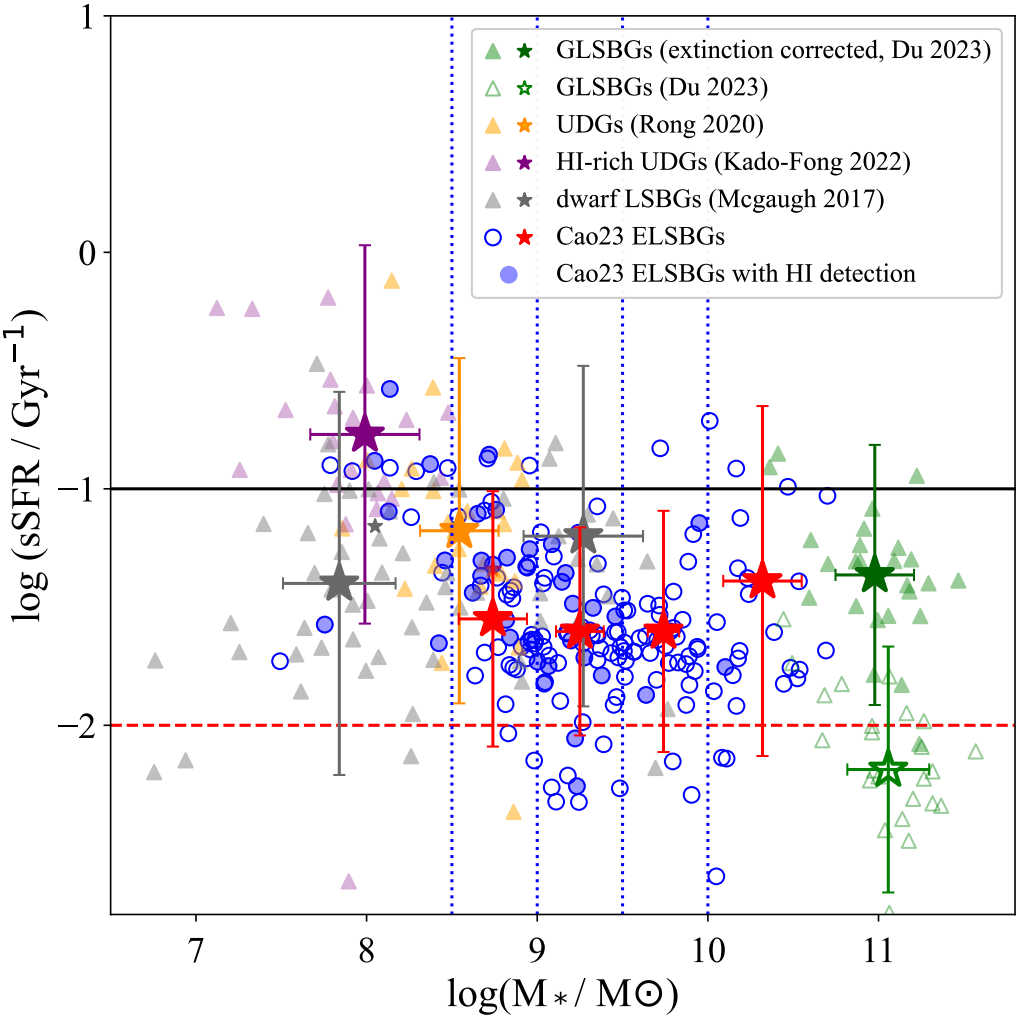

Figure 7. The sSFR-M_* relation for LSBGs. Blue open circles denote Cao23 ELSBGs, gray triangles represent dwarf LSBGs from [10], and orange triangles and plum triangles distinguish UDGs from [83,86], respectively. The blue dotted lines demarcate the boundaries of each stellar bin, with intervals of 0.5 dex in $\log(M_*/M_\odot)$ spanning from 8.5 to 10.5. Stellar masses falling below 8.5 and exceeding 10.5 are grouped into single bins, respectively. The red star symbols signify the mean values within each stellar bin. The black line is at $\log(\mathrm{sSFR/Gyr^{-1}}) = -1.0$. Furthermore, a red dashed line at $\log(\mathrm{sSFR/Gyr^{-1}}) = -2.0$ provides sSFR thresholds with passive galaxies typically falling below the red line. Purple and gray star symbols represent the mean values of HI-gas UDGs from [83] and dwarf LSBGs from [10] with $\log(M_*/M_\odot) < 8.5$. The IMF has been corrected to Chabrier IMF for all data points.

6. Non-Parametric Star-Formation History of Cao23 ELSBGs

Parametric models are widely employed for inferring the SFH of galaxies through the SED fitting technique [95]. However, this method relies on prior physical parameters [96,97]. The non-parametric SFH [98] assumes a constant SFR in each interval of a cosmic time grid instead of an exponential form of the SFR(t) [99–101].

We use the SED-fitting code PROSPECTOR [102] to fit the photometric data from an FUV to an NIR of 192 Cao23 ELSBGs. We adopt the non-parametric fixed-bin SFH models

preferred by [98]. The non-parametric fixed-bin SFH is described by a piecewise function where the SFR is a constant in each of the N time bins, and the edges of each time bin are fixed. The SFR in each fixed time bin is determined using the "continuity" prior, which places a Student-t prior on the log of the ratio of the SFR in adjacent bins (log SFR_{ratio}). We use the same N = 7 time bins (the edges are 0 Gyr, 0.03 Gyr, 0.1 Gyr, 0.33 Gyr, 1.1 Gyr, 3.6 Gyr, 11.6 Gyr, 13.7 Gyr) as [98] in our non-parametric SFH and apply [58] IMF. The dust type is chosen as the default power-law curve. The free parameters of dust attenuation and stellar metallicity apply flat priors over $0 < \tau_V < 3$ and $-2 < (\log Z/Z_{\odot}) < 0.19$. The redshift is fixed to SDSS spectroscopic redshift. We choose an ensemble Markov chain Monte Carlo (EMCMC, [102]) sampler to fit the model.

We compare the stellar mass assembly histories in different stellar bins. We show the on-average cumulative SFH in Figure 8. The low-mass ELSBGs ($10^{7.8} \leq M_* \leq 10^{9.0}\ M_{\odot}$) exhibit a slower stellar assembly history on average compared with high-mass ELSBGs ($M_* > 10^{9.0}\ M_{\odot}$). The low-mass galaxies build 80% of their stellar mass at look back time 1.4 Gyr, while the high-mass galaxies do so at look back time 3.7 Gyr. Low-mass ELSBGs assembled their 50% and 90% stellar masses at look back time 4.0 Gyr and 0.7 Gyr, respectively. High-mass ELSBGs assembled their 50% and 90% stellar masses at look back time 6.6 Gyr and 1.9 Gyr, respectively.

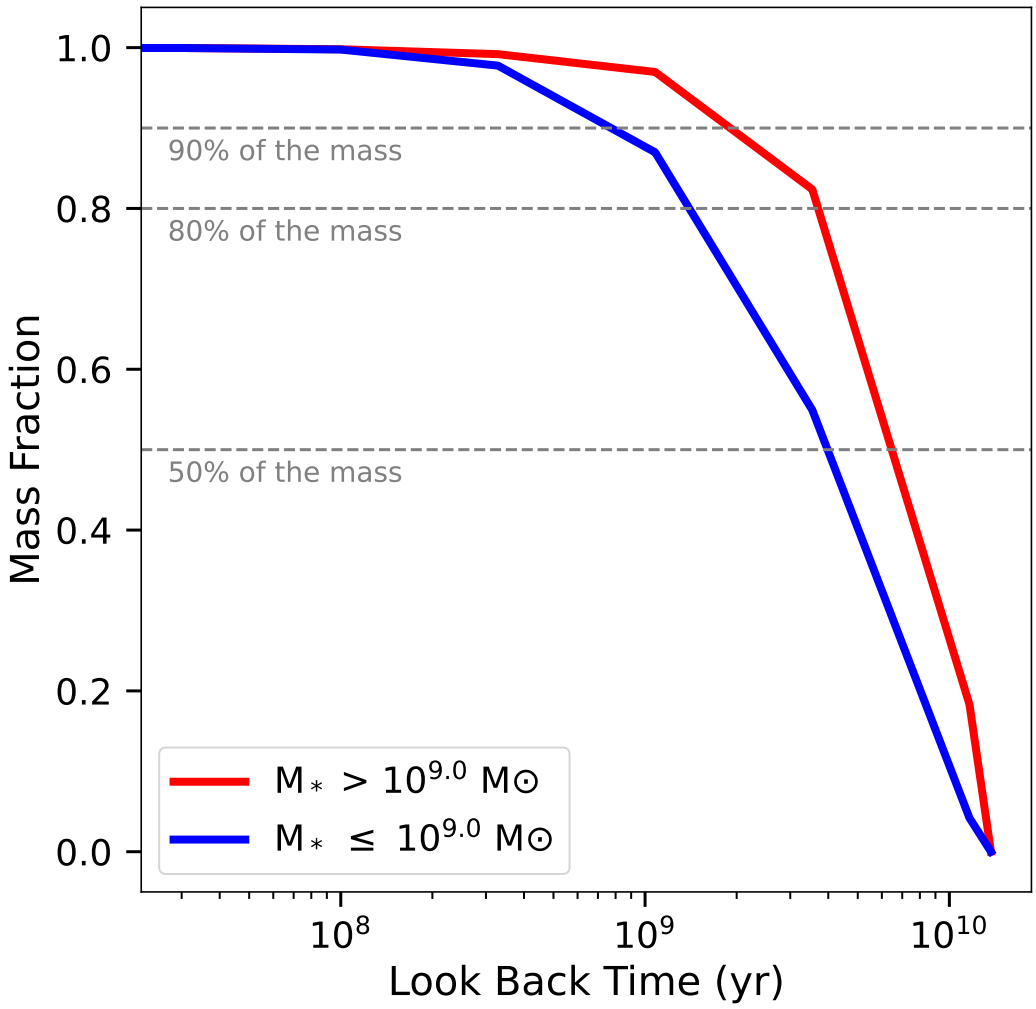

Figure 8. The mass growth curve through the look back times. The red line represents the mean value for those Cao23 ELSBGs with $M_* > 10^{9.0}\ M_{\odot}$, and the blue line represents the mean value for those Cao23 ELSBGs with $M_* \leq 10^{9.0}\ M_{\odot}$.

Figure 8 illustrates the downsizing paradigm in LSBGs. Theauthors of [23] analyzed the stellar population of Cao23 ELSBGs using SDSS fiber spectra, finding that more massive Cao23 ELSBGs are dominated by older stellar populations, supporting evidence for downsizing [103]. Ref. [104] noted an inverse correlation between galaxy mass and star formation duration (i.e., downsizing) by examing the [α/Fe] abundance with variable galaxy-wide IMF. Ref. [23] also show an α-enhancement in massive Cao23 ELSBGs, which is consistent with the downsizing trend [103,104]. Additionally, ref. [92] discussed the lower star formation efficiencies in more massive galaxies, and massive disk galaxies initiate star formation earlier than their low-mass counterparts with variable galaxy-wide IMF. The findings from Cao23 ELSBGs align with prior studies on normal spiral and elliptical galaxies [92,103–105]: massive LSBGs tend to have lower sSFRs, while low-mass ELSBGs form later than their massive counterparts. These results suggest that LSBGs share similar stellar build-up histories with normal galaxies.

7. Conclusions

This paper investigates the star formation rate and star formation history of ELSBGs from [23]. The principal outcomes are summarized as follows:

1. We compare Cao23 ELSBGs with HI-rich dwarf ELSBGs from [70] and super-thin (ST) galaxies from [73]. These ELSBGs have wide range luminosities ($-22 < M_r < -13$). The mean value of r_s for Cao23 ELSBGs is 3.19 $\pm$ 1.48 kpc, which is larger than that of HI-rich dwarf ELSBGs. Cao23 ELSBGs also show a redder (g-r) color than that of HI-rich dwarf ELSBGs. Cao23 ELSBGs are on average more massive ones compared to HI-rich dwarf LSBGs. We use the same method as [73] regarding the derived $\mathrm{SFR_{MAGPHYS}}$. Cao23 ELSBGs and STs share a similar position in the M_*-SFR relation. The comparison results suggest that Cao23 ELSBGs share similar properties with other LSBGs.

2. We estimated the SFR by WISE W3 luminosity and SED fitting methods. SFRs of Cao23 ELSBGs are below the main sequence in the M_*-SFR relation. The sSFR of ELSBGs are mainly in the range of 0.01–0.1 Gyr^{-1}.

3. The HI-rich dwarf LSBGs show larger sSFR and shorter t_{dep} values than low-HI gas fraction dwarf LSBGs, which means higher HI-gas content dwarf LSBGs tend to have higher SFRs. HI-rich dwarf LSBGs likely contain more molecular gas than their low HI-gas fraction counterparts, contributing to their higher sSFR. In contrast, GLSBGs and more massive Cao23 ELSBGs tend to have lower sSFR values on the sSFR-M_* relation.

4. We acquire the non-parametric SFHs of ELSBGs by SED fitting. The SFHs are divided into seven bins of look back time, and the SFR in each bin is assumed to be constant. We find that high-mass ($M_* > 10^{9.0}\ M_\odot$) ELSBGs assembled mass at an earlier time than that of low-mass ELSBGs. Combined with the results from the fiber spectra in [23], we conclude that our results support a downsizing trend for LSBGs.

Author Contributions: Conceptualization, methodology, and writing—original draft preparation J.W., T.-W.C., Z.-J.L. and P.-B.C.; writing—review and editing, visualization and supervision T.-W.C., V.M.K., C.C., G.G., J.W. and H.W. All authors have read and agreed to the published version of the manuscript.

Funding: J.W. acknowledges the National Key R&D Program of China (Grant No. 2023YFA1607904) and the National Natural Science Foundation of China (NSFC) grants 12033004, 12333002, and 12221003. T.C. acknowledges the China Postdoctoral Science Foundation (Grant No. 2023M742929) and the NSFC grants 12173045 and 12073051. G.G. acknowledges the ANID BASAL projects ACE210002 and FB210003. C.C. is supported by the NSFC, No. 11803044, 11933003, and 12173045 and acknowledge the science research grants from the China Manned Space Project with NO. CMS-CSST-2021-A05. H.W. acknowledges the NSFC grant No. 11733006 and 12090041. This work is sponsored (in part) by the Chinese Academy of Sciences (CAS) through a grant to the CAS South America Center for Astronomy (CASSACA). This work is supported (in part) by the NSFC, Nos. 12090040 and 12090041, and the Strategic Priority Research Program of the Chinese Academy of Sciences, Grant No. XDB0550100. JW is supported by the CNSA program D050102.

Data Availability Statement: The derived data generated in this research will be shared on reasonable request to the corresponding author.

Conflicts of Interest: The authors declare no conflicts of interest.

Appendix A

We list all of the input parameters settings of CIGALE used in Section 4.2.

Table A1. Parameters setting of each module in code CIGALE.

Modules	Parameters	Values
sfhdelayedbq	tau_main	500, 750, 1100, 1700, 2600 3900, 5800, 8800, 11000 (Myr)
	age_main	2000, 4500, 7000, 9500, 12000 (Myr)
	age_bq	0.0 (Myr)
	r_sfr	0.01, 0.03, 0.1, 0.3, 1.0, 3.0, 10
	sfr_A	1.0 ($M_{\odot}$yr^{-1})
bc03	imf	Chabrier
	metallicity	0.0001, 0.0004, 0.004, 0.008. ($M_{\odot}$)
	separation_age	10 (Myr)
nebular	logU	−2.0
distant_modified_starburst	E_BV_lines	0.0, 0.005, 0.0075, 0.011, 0.017, 0.026, 0.038, 0.058, 0.13, 0.2, 0.44, 0.66, 1.0 (mag)
	E_BV_factor	0.25, 0.50, 0.75
	Amplitude of the UV bump	0.0
	Powerlaw_slope	0.0
	Ext_law_emission_lines	Milky Way
	Rv	3.1
themis	qhac	0.02, 0.06, 0.10, 0.17, 0.24, 0.28
	umin	0.1,0.15,0.3,0.35,0.4 0.5,0.6,0.7,0.8,1.2,2.0
	alpha	2.0
	gamma	0.0, 0.001, 0.002, 0.004, 0.008 0.016, 0.031, 0.063, 0.13, 0.25, 0.5

References

1. Impey, C.; Bothun, G. Low Surface Brightness Galaxies. *Annu. Rev. Astron. Astrophys.* **1997**, *35*, 267–307. [CrossRef]
2. Bell, E.; Barnaby, D.; Bower, R.; De Jong, R.; Harper, D.; Hereld, M.; Loewenstein, R.; Rauscher, B. The star formation histories of low surface brightness galaxies. *Mon. Not. R. Astron. Soc. Lett.* **2000**, *312*, 470–496. [CrossRef]
3. Galaz, G.; Herrera-Camus, R.; Garcia-Lambas, D.; Padilla, N. Low Surface Brightness Galaxies in the SDSS: The Link Between Environment, Star-forming Properties, and Active Galactic Nuclei. *Astrophys. J.* **2011**, *728*, e74. [CrossRef]
4. Cheng, C.; Du, W.; Xu, C.; Cao, T.; Zhang, H.; Huang, J.; He, C.; Li, Z.; Wu, S.; Xu, H.; et al. FUV and NIR size of the HI selected low surface brightness galaxies. *Res. Astron. Astrophys.* **2021**, *21*, e076. [CrossRef]
5. Lei, F.; Wu, H. Examining the Influence of the Regions on Star Formation Surface Density. *Publ. Astron. Soc. Pac.* **2023**, *135*, e104101. [CrossRef]
6. Zhang, B.; Wu, H.; Du, W.; Zhao, P.; He, M.; Lei, F. Low Surface Brightness Galaxies Selected by Different Model Fitting. *Res. Astron. Astrophys.* **2024**, *24*, e015018. [CrossRef]
7. Du, L.; Du, W.; Cheng, C.; Zhu, M.; Yu, H.; Wu, H. Almost Optically Dark Galaxies in DECaLS (I): Detection, Optical Properties, and Possible Origins. *Astrophys. J.* **2024**, *964*, e85. [CrossRef]
8. Tang, L. Stellar metallicity of galaxies: New insight on the formation and evolution of Low Surface Brightness Galaxies in the IllustrisTNG simulation. *Mon. Not. R. Astron. Soc.* **2024**, *530*, stae845. [CrossRef]

9. Du, P.; Du, W.; Zhang, B.; Yi, Z.; He, M.; Wu, H. Low Surface Brightness Galaxies from BASS+MzLS with Machine Learning. *Res. Astron. Astrophys.* **2024**, *24*, e055015. [CrossRef]
10. McGaugh, S.; Schombert, J.; Lelli, F. The Star-forming Main Sequence of Dwarf Low Surface Brightness Galaxies. *Astrophys. J.* **2017**, *851*, e22. [CrossRef]
11. Van Dokkum, P.; Abraham, R.; Merritt, A.; Zhang, J.; Geha, M.; Conroy, C. Forty-seven Milky Way-sized, Extremely Diffuse Galaxies in the Coma Cluster. *Astrophys. J. Lett.* **2015**, *798*, eL45. [CrossRef]
12. Van Dokkum, P.; Romanowsky, A.; Abraham, R.; Brodie, J.; Conroy, C.; Geha, M.; Merritt, A.; Villaume, A.; Zhang, J. Spectroscopic Confirmation of the Existence of Large, Diffuse Galaxies in the Coma Cluster. *Astrophys. J. Lett.* **2015**, *804*, eL26. [CrossRef]
13. Bothun, G.; Impey, C.; Malin, D.; Mould, J. Discovery of a Huge Low-Surface-Brightness Galaxy: A Proto-Disk Galaxy at Low Redshift? *Astron. J.* **1987**, *94*, 23. [CrossRef]
14. Galaz, G.; Milovic, C.; Suc, V.; Busta, L.; Lizana, G.; Infante, L.; Royo, S. Deep Optical Images of Malin 1 Reveal New Features. *Astrophys. J. Lett.* **2015**, *815*, eL29. [CrossRef]
15. Boissier, S.; Boselli, A.; Ferrarese, L.; Côté, P.; Roehlly, Y.; Gwyn, S.D.; Cuillandre, J.C.; Roediger, J.; Koda, J.; Mateos, J.M.; et al. The properties of the Malin 1 galaxy giant disk. A panchromatic view from the NGVS and GUViCS surveys. *Astron. Astrophys.* **2016**, *593*, eA126. [CrossRef]
16. Saburova, A.; Chilingarian, I.; Kulier, A.; Galaz, G.; Grishin, K.; Kasparova, A.; Toptun, V.; Katkov, I. The volume density of giant low surface brightness galaxies. *Mon. Not. R. Astron. Soc.* **2023**, *520*, L85–L90. [CrossRef]
17. Johnston, E.; Galaz, G.; Blaña, M.; Amram, P.; Boissier, S.; Eigenthaler, P.; Epinat, B.; Junais, O.-B.Y.; Puzia, T.; Weilbacher, P. A MUSE view of the core of the giant low-surface-brightness galaxy Malin 1. *Astron. Astrophys.* **2024**, *686*, eA247. [CrossRef]
18. Saburova, A.; Gasymov, D.; Rubtsov, E.; Chilingarian, I.; Borisov, S.; Gerasimov, I.; Kolganov, F.; Kasparova, A.; Uklein, R.; Bilek, M.; et al. A Closer Look at the Extended Edge-on Low-surface Brightness Galaxies. *Astrophys. J.* **2024**, *973*, e167. [CrossRef]
19. De Blok, W.; McGaugh, S. Does Low Surface Brightness Mean Low Density? *Astrophys. J. Lett.* **1996**, *469*, L89. [CrossRef]
20. Kuzio de Naray, R.; McGaugh, S.; De Blok, W. Oxygen abundances and chemical evolution in low surface brightness galaxies. *Mon. Not. R. Astron. Soc.* **2004**, *355*, 887–898. [CrossRef]
21. Du, W.; Wu, H.; Zhu, Y.; Zheng, W.; Filippenko, A. Long-slit Spectroscopy of Edge-on Low Surface Brightness Galaxies. *Astrophys. J.* **2017**, *837*, e152. [CrossRef]
22. Cao, T.; Li, Z.; Chen, P.; Zhang, C.; Galaz, G.; Cheng, C.; Yu, Q.; Kalari, V.; Wang, J.; Wu, H. Ionized and Cold Gas Components in Low Surface Brightness Galaxy AGC 102004. *Astrophys. J.* **2024**, *971*, 181. [CrossRef]
23. Cao, T.; Wu, H.; Galaz, G.; Kalari, V.; Cheng, C.; Li, Z.; Wang, J. Understanding the Chemical Evolution of Blue Edge-on Low Surface Brightness Galaxies. *Astrophys. J.* **2023**, *948*, e96. [CrossRef]
24. Wyder, T.; Martin, D.; Barlow, T.; Foster, K.; Friedman, P.; Morrissey, P.; Neff, S.; Neill, J.; Schiminovich, D.; Seibert, M.; et al. The Star Formation Law at Low Surface Density. *Astrophys. J.* **2009**, *696*, 1834–1853. [CrossRef]
25. Lei, F.; Wu, H.; Du, W.; Zhu, Y.; Lam, M.; Zhou, Z.; He, M.; Jin, J.; Cao, T.; Zhao, P.; et al. An Hα Imaging Survey of the Low-surface-brightness Galaxies Selected from the Fall Sky Region of the 40% ALFALFA H I Survey. *Astrophys. J. Suppl. Ser.* **2018**, *235*, e18. [CrossRef]
26. Lei, F.; Wu, H.; Zhu, Y.; Du, W.; He, M.; Jin, J.; Zhao, P.; Zhang, B. An Hα Imaging Survey of the Low Surface Brightness Galaxies Selected from the Spring Sky Region of the 40% ALFALFA H I Survey. *Astrophys. J. Suppl. Ser.* **2019**, *242*, e11. [CrossRef]
27. Rahman, N.; Howell, J.; Helou, G.; Mazzarella, J.; Buckalew, B. Exploring Infrared Properties of Giant Low Surface Brightness Galaxies. *Astrophys. J.* **2007**, *663*, 908–923. [CrossRef]
28. Hinz, J.; Rieke, M.; Rieke, G.; Willmer, C.; Misselt, K.; Engelbracht, C.; Blaylock, M.; Pickering, T. Spitzer Observations of Low-Luminosity Isolated and Low Surface Brightness Galaxies. *Astrophys. J.* **2007**, *663*, 895–907. [CrossRef]
29. Junais, J.; Małek, K.; Boissier, S.; Pearson, W.J.; Pollo, A.; Boselli, A.; Boquien, M.; Donevski, D.; Goto, T.; Hamed, M.; et al. Variation in optical and infrared properties of galaxies in relation to their surface brightness. *Astron. Astrophys.* **2023**, *676*, eA41. [CrossRef]
30. Matthews, L.; Gao, Y. CO Detections of Edge-on Low Surface Brightness Galaxies. *Astrophys. J. Lett.* **2001**, *549*, L191–L194. [CrossRef]
31. Cao, T.; Wu, H.; Du, W.; Lei, F.; Zhu, M.; Wouterloot, J.; Parsons, H.; Zhu, Y.; Wu, C.; Yang, F.; et al. Molecular Gas and Star-formation in Low Surface Brightness Galaxies. *Astron. J.* **2017**, *154*, e116. [CrossRef]
32. Galaz, G.; Gonzalez-Lopez, J.; Guzman, V.; Messias, H.; Junais Boissier, S.; Epinat, B.; Weilbacher, P.; Puzia, T.; Johnston, E.; Amram, P.; et al. First Detection of Molecular Gas in the Giant Low Surface Brightness Galaxy Malin 1. *arXiv* **2024**, arXiv:2410.22230. [CrossRef]
33. Du, W.; Wu, H.; Lam, M.; Zhu, Y.; Lei, F.; Zhou, Z. Low Surface Brightness Galaxies Selected from the 40% Sky Area of the ALFALFA H I Survey. I. Sample and Statistical Properties. *Astron. J.* **2015**, *149*, e199. [CrossRef]
34. Parkash, V.; Brown, M.; Jarrett, T.; Bonne, N. Relationships between HI Gas Mass, Stellar Mass, and the Star Formation Rate of HICAT+WISE (H I-WISE) Galaxies. *Astrophys. J.* **2018**, *864*, e40. [CrossRef]
35. Du, W.; Cheng, C.; Du, P.; Du, L.; Wu, H. Star-forming Main Sequence of Giant Low Surface Brightness Galaxies. *Astrophys. J.* **2023**, *959*, e105. [CrossRef]
36. Ogiya, G. Tidal stripping as a possible origin of the ultra diffuse galaxy lacking dark matter. *Mon. Not. R. Astron. Soc. Lett.* **2018**, *480*, L106–L110. [CrossRef]

37. Rong, Y.; Dong, X.; Puzia, T.; Galaz, G.; Sánchez-Janssen, R.; Cao, T.; Van der Burg, R.; Sifón, C.; Mancera Piña, P.; Marcelo, M.; et al. Intrinsic Morphology of Ultra-diffuse Galaxies. *Astrophys. J.* **2020**, *899*, e78. [CrossRef]
38. Kulier, A.; Galaz, G.; Padilla, N.; Trayford, J. Massive low-surface-brightness galaxies in the EAGLE simulation. *Mon. Not. R. Astron. Soc. Lett.* **2020**, *496*, 3996–4016. [CrossRef]
39. Junais, J.; Boissier, S.; Boselli, A.; Ferrarese, L.; Côté, P.; Gwyn, S.; Roediger, J.; Lim, S.; Peng, E.W.; Cuill, J.C.; et al. A Virgo Environmental Survey Tracing Ionised Gas Emission (VESTIGE). XIII. The role of ram-pressure stripping in transforming the diffuse and ultra-diffuse galaxies in the Virgo cluster. *Astron. Astrophys.* **2022**, *667*, eA76. [CrossRef]
40. Dalcanton, J.; Spergel, D.; Summers, F. The Formation of Disk Galaxies. *Astrophys. J.* **1997**, *482*, 659–676. [CrossRef]
41. Pérez-Montaño, L.E.; Rodriguez-Gomez, V.; Cervantes Sodi, B.; Zhu, Q.; Pillepich, A.; Vogelsberger, M.; Hernquist, L. The formation of low surface brightness galaxies in the IllustrisTNG simulation. *Mon. Not. R. Astron. Soc. Lett.* **2022**, *514*, 5840–5852. [CrossRef]
42. Martin, G.; Kaviraj, S.; Laigle, C.; Devriendt, J.; Jackson, R.; Peirani, S.; Dubois, Y.; Pichon, C.; Slyz, A. The formation and evolution of low-surface-brightness galaxies. *Mon. Not. R. Astron. Soc. Lett.* **2019**, *485*, 796–818. [CrossRef]
43. Jackson, R.; Martin, G.; Kaviraj, S.; Ramsøy, M.; Devriendt, J.; Sedgwick, T.; Laigle, C.; Choi, H.; Beckmann, R.; Volonteri, M.; et al. The origin of low-surface-brightness galaxies in the dwarf regime. *Mon. Not. R. Astron. Soc. Lett.* **2021**, *502*, 4262–4276. [CrossRef]
44. Wright, A.; Tremmel, M.; Brooks, A.; Munshi, F.; Nagai, D.; Sharma, R.; Quinn, T. The formation of isolated ultradiffuse galaxies in ROMULUS25. *Mon. Not. R. Astron. Soc. Lett.* **2021**, *502*, 5370–5389. [CrossRef]
45. Saburova, A.; Chilingarian, I.; Kasparova, A.; Sil'chenko, O.; Grishin, K.; Katkov, I.; Uklein, R. Observational insights on the origin of giant low surface brightness galaxies. *Mon. Not. R. Astron. Soc. Lett.* **2021**, *503*, 830–849. [CrossRef]
46. Zhu, Q.; Pérez-Montaño, L.; Rodriguez-Gomez, V.; Cervantes, S.B.; Zjupa, J.; Marinacci, F.; Vogelsberger, M.; Hernquist, L. Giant low surface brightness galaxies in TNG100. *Mon. Not. R. Astron. Soc. Lett.* **2023**, *523*, 3991–4014. [CrossRef]
47. Hu, J.; Xu, D.; Li, C. Formation of super-thin galaxies in Illustris-TNG. *arXiv* **2024**, arXiv:2406.13745v1.
48. Brinchmann, J.; Ellis, R. The Mass Assembly and Star Formation Characteristics of Field Galaxies of Known Morphology. *Astrophys. J.* **2000**, *536*, L77–L80. [CrossRef]
49. Sandles, L.; Curtis-Lake, E.; Charlot, S.; Chevallard, J.; Maiolino, R. Bayesian hierarchical modelling of the M_*-SFR relation from $1 \lesssim z \lesssim 6$ in ASTRODEEP. *Mon. Not. R. Astron. Soc. Lett.* **2022**, *515*, 2951–2969. [CrossRef]
50. Feulner, G.; Goranova, Y.; Drory, N.; Hopp, U.; Bender, R. The connection between star formation and stellar mass: Specific star formation rates to redshift one. *Mon. Not. R. Astron. Soc. Lett.* **2005**, *358*, L1–L5. [CrossRef]
51. Tasca, L.; Le Fèvre, O.; Hathi, N.; Schaerer, D.; Ilbert, O.; Zamorani, G.; Lemaux, B.; Cassata, P.; Garilli, B.; Le Brun, V.; et al. The evolving star formation rate: M_* relation and sSFR since $z \simeq 5$ from the VUDS spectroscopic survey. *Astron. Astrophys.* **2015**, *581*, eA54. [CrossRef]
52. Ocran, E.; Vaccari, M.; Stil, J.; Taylor, A.; Ishwara-Ch, C.; Kim, J. Star formation history of $0.1 \leq z \leq 1.5$ mass-selected galaxies in the ELAIS-N1 Field. *Mon. Not. R. Astron. Soc. Lett.* **2023**, *524*, 5229–5247. [CrossRef]
53. Neistein, E.; Van den Bosch, F.; Dekel, A. Natural downsizing in hierarchical galaxy formation. *Mon. Not. R. Astron. Soc. Lett.* **2006**, *372*, 933–948. [CrossRef]
54. Carleton, T.; Cohen, S.; Frye, B.; Pigarelli, A.; Zhang, J.; Windhorst, R.; Diego, J.; Conselice, C.; Cheng, C.; Driver, S.; et al. PEARLS: Low Stellar Density Galaxies in the El Gordo Cluster Observed with JWST. *Astrophys. J.* **2023**, *953*, e83. [CrossRef]
55. Zhao, P.; Liu, F.; Cui, Q.; Yesuf, H.; Wu, H. Structure and Color Gradients of Ultradiffuse Galaxies in Distant Massive Galaxy Clusters. *Astrophys. J.* **2024**, *960*, e9. [CrossRef]
56. Pflamm-Altenburg, J.; Kroupa, P. The Fundamental Gas Depletion and Stellar-Mass Buildup Times of Star-Forming Galaxies. *Astrophys. J.* **2009**, *706*, 516–524. [CrossRef]
57. Kauffmann, G.; Heckman, T.; White, S.; Charlot, S.; Tremonti, C.; Brinchmann, J.; Bruzual, G.; Peng, E.; Seibert, M.; Bernardi, M.; et al. Stellar masses and star formation histories for 10^5 galaxies from the Sloan Digital Sky Survey. *Mon. Not. R. Astron. Soc. Lett.* **2003**, *341*, 33–53. [CrossRef]
58. Chabrier, G. Galactic Stellar and Substellar Initial Mass Function. *Publ. Astron. Soc. Pac.* **2003**, *115*, 763–795. [CrossRef]
59. Salpeter, E. The Luminosity Function and Stellar Evolution. *Astrophys. J.* **1955**, *121*, 161. [CrossRef]
60. Kroupa, P. On the variation of the initial mass function. *Mon. Not. R. Astron. Soc. Lett.* **2001**, *322*, 231–246. [CrossRef]
61. Elbaz, D.; Daddi, E.; Le Borgne, D.; Dickinson, M.; Alexander, D.M.; Chary, R.R.; Starck, J.L.; Brandt, W.N.; Kitzbichler, M.; MacDonald, E.; et al. The reversal of the star formation-density relation in the distant universe. *Astron. Astrophys.* **2007**, *468*, 33–48. [CrossRef]
62. Davé, R. The galaxy stellar mass-star formation rate relation: Evidence for an evolving stellar initial mass function? *Mon. Not. R. Astron. Soc. Lett.* **2008**, *385*, 147–160. [CrossRef]
63. Santini, P.; Maiolino, R.; Magnelli, B.; Lutz, D.; Lamastra, A.; Li Causi, G.; Eales, S.; Andreani, P.; Berta, S.; Buat, V.; et al. The evolution of the dust and gas content in galaxies. *Astron. Astrophys.* **2014**, *562*, eA30. [CrossRef]
64. Duarte Puertas, S.; Vilchez, J.; Iglesias-Páramo, J.; Kehrig, C.; Pérez-Montero, E.; Rosales-Ortega, F. Aperture-free star formation rate of SDSS star-forming galaxies. *Astron. Astrophys.* **2017**, *599*, eA71. [CrossRef]
65. Simard, L.; Mendel, J.; Patton, D.; Ellison, S.; McConnachie, A. A Catalog of Bulge+disk Decompositions and Updated Photometry for 1.12 Million Galaxies in the Sloan Digital Sky Survey. *Astrophys. J. Suppl. Ser.* **2011**, *196*, e11. [CrossRef]

66. Van Velzen, S.; Gezari, S.; Hammerstein, E.; Roth, N.; Frederick, S.; Ward, C.; Hung, T.; Cenko, S.; Stein, R.; Perley, D.; et al. Seventeen Tidal Disruption Events from the First Half of ZTF Survey Observations: Entering a New Era of Population Studies. *Astrophys. J.* **2021**, *908*, e4. [CrossRef]
67. Van der Kruit, P.; Searle, L. Surface photometry of edge-on spiral galaxies. I–A model for the three-dimensional distribution of light in galactic disks. *Astron. Astrophys.* **1981**, *95*, 105–115.
68. Giovanelli, R.; Haynes, M.; Salzer, J.; Wegner, G.; Da Costa, L.; Freudling, W. Dependence on Luminosity of Photometric Properties of Disk Galaxies: Surface Brightness, Size, and Internal Extinction. *Astron. J.* **1995**, *110*, 1059. [CrossRef]
69. He, M.; Wu, H.; Du, W.; Wicker, J.; Zhao, P.; Lei, F.; Liu, J. Edge-on H I-bearing Ultra-diffuse Galaxy Candidates in the 40% ALFALFA Catalog. *Astrophys. J.* **2019**, *880*, e30. [CrossRef]
70. He, M.; Wu, H.; Du, W.; Liu, H.; Lei, F.; Zhao, P.; Zhang, B. A Sample of Edge-on H I-rich Low Surface Brightness Galaxy Candidates in the 40% ALFALFA Catalog. *Astrophys. J. Suppl. Ser.* **2020**, *248*, e33. [CrossRef]
71. Greco, J.; Greene, J.; Strauss, M.; Macarthur, L.; Flowers, X.; Goulding, A.; Huang, S.; Kim, J.; Komiyama, Y.; Leauthaud, A.; et al. Illuminating Low Surface Brightness Galaxies with the Hyper Suprime-Cam Survey. *Astrophys. J.* **2018**, *857*, e104. [CrossRef]
72. Tanoglidis, D.; Drlica-Wagner, A.; Wei, K.; Li, T.S.; Sánchez, J.; Zhang, Y.; Peter, A.H.; Feldmeier-Krause, A.; Prat, J.; Casey, K.; et al. Shadows in the Dark: Low-surface-brightness Galaxies Discovered in the Dark Energy Survey. *Astrophys. J. Suppl. Ser.* **2021**, *252*, e18. [CrossRef]
73. Narayanan, G.; Banerjee, A. Are superthin galaxies low-surface-brightness galaxies seen edge-on? The star formation probe. *Mon. Not. R. Astron. Soc. Lett.* **2022**, *514*, 5126–5140. [CrossRef]
74. Da Cunha, E.; Charlot, S.; Elbaz, D. A simple model to interpret the ultraviolet, optical and infrared emission from galaxies. *Mon. Not. R. Astron. Soc. Lett.* **2008**, *388*, 1595–1617. [CrossRef]
75. Bruzual, G.; Charlot, S. Stellar population synthesis at the resolution of 2003. *Mon. Not. R. Astron. Soc. Lett.* **2003**, *344*, 1000–1028. [CrossRef]
76. Charlot, S.; Fall, S. A Simple Model for the Absorption of Starlight by Dust in Galaxies. *Astrophys. J.* **2000**, *539*, 718–731. [CrossRef]
77. Hunt, L.; De Looze, I.; Boquien, M.; Nikutta, R.; Rossi, A.; Bianchi, S.; Dale, D.; Granato, G.; Kennicutt, R.; Silva, L.; et al. Comprehensive comparison of models for spectral energy distributions from 0.1 μm to 1 mm of nearby star-forming galaxies. *Astron. Astrophys.* **2019**, *621*, eA51. [CrossRef]
78. Shipley, H.; Papovich, C.; Rieke, G.; Brown, M.; Moustakas, J. A New Star Formation Rate Calibration from Polycyclic Aromatic Hydrocarbon Emission Features and Application to High-redshift Galaxies. *Astrophys. J.* **2016**, *818*, e60. [CrossRef]
79. Davies, L.; Driver, S.; Robotham, A.; Grootes, M.; Popescu, C.; Tuffs, R.; Hopkins, A.; Alpaslan, M.; Andrews, S.; Bland-Hawthorn, J.; et al. GAMA/H-ATLAS: A meta-analysis of SFR indicators - comprehensive measures of the SFR-M$|^*$ relation and cosmic star formation history at z < 0.4. *Mon. Not. R. Astron. Soc. Lett.* **2016**, *461*, 458–485.
80. Beom, M.; Bizyaev, D.; Walterbos, R.; Chen, Y. SDSS IV MaNGA: Characteristics of edge-on galaxies with a counter-rotating gaseous disc. *Mon. Not. R. Astron. Soc. Lett.* **2022**, *516*, 3175–3192. [CrossRef]
81. Boquien, M.; Burgarella, D.; Roehlly, Y.; Buat, V.; Ciesla, L.; Corre, D.; Inoue, A.; Salas, H. CIGALE: A python Code Investigating GALaxy Emission. *Astron. Astrophys.* **2019**, *622*, eA103. [CrossRef]
82. Chen, P.; Zhao, Y.; Wang, J. The Unusual AGN Host NGC 1266: Evidence for Shocks in a Molecular Gas Rich S0 Galaxy with a Low Luminosity Nucleus. *Res. Astron. Astrophys.* **2023**, *23*, e015005. [CrossRef]
83. Kado-Fong, E.; Greene, J.; Huang, S.; Goulding, A. Ultra-diffuse Galaxies as Extreme Star-forming Environments. I. Mapping Star Formation in H I-rich UDGs. *Astrophys. J.* **2022**, *941*, e11. [CrossRef]
84. Jones, A.; Köhler, M.; Ysard, N.; Bocchio, M.; Verstraete, L. The global dust modelling framework THEMIS. *Astron. Astrophys.* **2017**, *602*, eA46. [CrossRef]
85. Calzetti, D.; Armus, L.; Bohlin, R.; Kinney, A.; Koornneef, J.; Storchi-Bergmann, T. The Dust Content and Opacity of Actively Star-forming Galaxies. *Astrophys. J.* **2000**, *533*, 682–695. [CrossRef]
86. Rong, Y.; Zhu, K.; Johnston, E.; Zhang, H.; Cao, T.; Puzia, T.; Galaz, G. Lessons on Star-forming Ultra-diffuse Galaxies from the Stacked Spectra of the Sloan Digital Sky Survey. *Astrophys. J. Lett.* **2020**, *899*, eL12. [CrossRef]
87. Di Teodoro, E.; Posti, L.; Ogle, P.; Fall, S.; Jarrett, T. Rotation curves and scaling relations of extremely massive spiral galaxies. *Mon. Not. R. Astron. Soc. Lett.* **2021**, *507*, 5820–5831. [CrossRef]
88. Speagle, J.; Steinhardt, C.; Capak, P.; Silverman, J. A Highly Consistent Framework for the Evolution of the Star-Forming "Main Sequence" from z ∼0–6. *Astrophys. J. Suppl. Ser.* **2014**, *214*, e15. [CrossRef]
89. Saintonge, A.; Catinella, B.; Cortese, L.; Genzel, R.; Giovanelli, R.; Haynes, M.; Janowiecki, S.; Kramer, C.; Lutz, K.; Schiminovich, D.; et al. Molecular and atomic gas along and across the main sequence of star-forming galaxies. *Mon. Not. R. Astron. Soc. Lett.* **2016**, *462*, 1749–1756. [CrossRef]
90. Jeřábková, T.; Hasani, Z.A.; Kroupa, P.; Beccari, G.; Yan, Z.; Vazdekis, A.; Zhang, Z. Impact of metallicity and star formation rate on the time-dependent, galaxy-wide stellar initial mass function. *Astron. Astrophys.* **2018**, *620*, eA39. [CrossRef]
91. Kroupa, P.; Gjergo, E.; Jerabkova, T.; Yan, Z. The initial mass function of stars. *arXiv* **2024**, arXiv:2410.07311.
92. Haslbauer, M.; Yan, Z.; Jerabkova, T.; Gjergo, E.; Kroupa, P.; Hasani, Z.A. The effect of the environment-dependent stellar initial mass function on the photometric properties of star-forming galaxies. *Astron. Astrophys.* **2024**, *689*, eA221. [CrossRef]
93. Dobbels, W.; Baes, M.; Viaene, S.; Bianchi, S.; Davies, J.; Casasola, V.; Clark, C.; Fritz, J.; Galametz, M.; Galliano, F.; et al. Predicting the global far-infrared SED of galaxies via machine learning techniques. *Astron. Astrophys.* **2020**, *634*, eA57. [CrossRef]

94. Haskell, P.; Smith, D.; Cochrane, R.; Hayward, C.; Anglés-Alcázar, D. Energy balance SED modelling can be effective at high redshifts regardless of UV-FIR offsets. *Mon. Not. R. Astron. Soc. Lett.* **2023**, *525*, 1535–1552. [CrossRef]
95. Conroy, C. Modeling the Panchromatic Spectral Energy Distributions of Galaxies. *Annu. Rev. Astron. Astrophys.* **2013**, *51*, 393–455. [CrossRef]
96. Carnall, A.; Leja, J.; Johnson, B.; McLure, R.; Dunlop, J.; Conroy, C. How to Measure Galaxy Star Formation Histories. I. Parametric Models. *Astrophys. J.* **2019**, *873*, e44. [CrossRef]
97. Pappalardo, C.; Cardoso, L.; Michel Gomes, J.; Papaderos, P.; Afonso, J.; Breda, I.; Humphrey, A.; Scott, T.; Amarantidis, S.; Matute, I.; et al. Self-consistent population spectral synthesis with FADO. II. Star formation history of galaxies in spectral synthesis methods. *Astron. Astrophys.* **2021**, *651*, eA99. [CrossRef]
98. Leja, J.; Carnall, A.; Johnson, B.; Conroy, C.; Speagle, J. How to Measure Galaxy Star Formation Histories. II. Nonparametric Models. *Astrophys. J.* **2019**, *876*, e3. [CrossRef]
99. Fernandes, R.C.; Mateus, A.; Sodré, L.; Stasińska, G.; Gomes, J.M. Semi-empirical analysis of Sloan Digital Sky Survey galaxies - I. Spectral synthesis method. *Mon. Not. R. Astron. Soc. Lett.* **2005**, *358*, 363–378. [CrossRef]
100. Leja, J.; Johnson, B.; Conroy, C.; Van Dokkum, P.; Byler, N. Deriving Physical Properties from Broadband Photometry with Prospector: Description of the Model and a Demonstration of its Accuracy Using 129 Galaxies in the Local Universe. *Astrophys. J.* **2017**, *837*, e170. [CrossRef]
101. Chauke, P.; Van der Wel, A.; Pacifici, C.; Bezanson, R.; Wu, P.; Gallazzi, A.; Noeske, K.; Straatman, C.; Muños-Mateos, J.; Franx, M.; et al. Star Formation Histories of z ∼1 Galaxies in LEGA-C. *Astrophys. J.* **2018**, *861*, e13. [CrossRef]
102. Johnson, B.; Leja, J.; Conroy, C.; Speagle, J. Stellar Population Inference with Prospector. *Astrophys. J. Suppl. Ser.* **2021**, *254*, e22. [CrossRef]
103. Fontanot, F.; De Lucia, G.; Monaco, P.; Somerville, R.; Santini, P. The many manifestations of downsizing: Hierarchical galaxy formation models confront observations. *Mon. Not. R. Astron. Soc. Lett.* **2009**, *397*, 1776–1790. [CrossRef]
104. Recchi, S.; Calura, F.; Kroupa, P. The chemical evolution of galaxies within the IGIMF theory: The [α/Fe] ratios and downsizing. *Astron. Astrophys.* **2009**, *499*, 711–722. [CrossRef]
105. Yan, Z.; Jeřábková, T.; Kroupa, P. Downsizing revised: Star formation timescales for elliptical galaxies with an environment-dependent IMF and a number of SNIa. *Astron. Astrophys.* **2021**, *655*, eA19. [CrossRef]